



Reynolds-number scaling of vortex pinch-off on low-aspect-ratio propulsors

John N. Fernando^{1,†} and David E. Rival¹

¹Department of Mechanical and Materials Engineering, Queen's University, Kingston, ON K7L 3N6, Canada

(Received 1 April 2016; revised 3 May 2016; accepted 6 June 2016; first published online 23 June 2016)

Impulsively started, low-aspect-ratio elliptical flat plates have been investigated experimentally to understand the vortex pinch-off dynamics at transitional and fully turbulent Reynolds numbers. The range of Reynolds numbers investigated is representative of those observed in animals that employ rowing and paddling modes of drag-based propulsion and manoeuvring. Elliptical flat plates with five aspect ratios ranging from one to two have been considered, as abstractions of propulsor planforms found in nature. It has been shown that Reynolds-number scaling is primarily determined by plate aspect ratio in terms of both drag forces and vortex pinch-off. Due to vortex-ring growth time scales that are longer than those associated with the development of flow instabilities, the scaling of drag is Reynolds-number-dependent for the aspect-ratio-one flat plate. With increasing aspect ratio, the Reynolds-number dependency decreases as a result of the shorter growth time scales associated with high-aspect-ratio elliptical vortex rings. Large drag peaks are observed during early-stage vortex growth for the higher-aspect-ratio flat plates. The collapse of these peaks with Reynolds number provides insight into the evolutionary convergence process of propulsor planforms used in drag-based swimming modes over diverse scales towards aspect ratios greater than one.

Key words: propulsion, swimming/flying, vortex dynamics

1. Introduction

The similarities in body morphology and locomotory modes observed in species with distinct taxonomies have become quintessential examples of evolutionary convergence (Lighthill 1969). Among the numerous swimming and flying species, this convergence is manifested in the overall body shapes and appendage profiles found over a broad range of biological scales, and in the two locomotory modes of lift-based and drag-based propulsion (Vogel 2013).

† Email address for correspondence: john.fernando@queensu.ca

In a seminal study on the hydromechanics of animal propulsion, Lighthill (1969) investigated the evolution of swimming techniques employed by fish involving varying degrees of transverse body compression, as well as appendage shape. It was suggested in this study that the convergence of caudal fins observed in carangiform swimmers towards similar lunate shapes is based on structural constraints. However, more recent studies have suggested that structural constraints may not be as important, and that vorticity generation and shedding is the primary feature of optimization (Gazzola, Van Rees & Koumoutsakos 2012; Eloy 2013). As such, in order to gain insight into the convergence of appendage profiles found in nature, Hartloper & Rival (2013) compared leading-edge vortex growth between flat plates with and without curvature. The wake generated in the presence of leading-edge curvature was found to be associated with optimal lift-to-drag ratios, which has shed additional light on the evolutionary convergence towards spanwise leading-edge curvature in biological appendages undergoing lift-based manoeuvres.

Drag-based modes of propulsion have been linked with low-speed locomotion due to the large generation of thrust possible over short time intervals (Vogel 2013). In other words, drag-based swimming modes are preferred during quick accelerations, and while turning and braking. Specific examples of drag-based propulsion in nature are generally accompanied by factors that increase the complexity of analyses, such as propulsor deformation, propulsor–body interaction, and rapid-area change of propulsors during recovery strokes to reduce drag (Blake 1979, 1981). Despite these added complexities, recent studies have considered abstractions of commonly observed propulsor geometries and kinematics to generalize the insight gained. Kim & Gharib (2011) investigated the relationship between vortex formation and thrust generation of rectangular, triangular, and delta-shaped flat plates (rigid and flexible) undergoing a simplified power-stroke motion. Thrust production was shown to be strongly correlated with spanwise flow, which was observed to the largest extent in the delta-shaped flat plate. Propulsor flexibility was also shown to damp out large thrust peaks during sudden motions, which is important in minimizing structural loading and stabilizing body motion. Fernando & Rival (2016) abstracted the motion of a propulsor during a drag-based manoeuvre with several flat plates undergoing rectilinear motions normal to the fluid. Elliptical and rectangular flat plates with aspect ratios of one, two, three, and four were considered, to determine the influence of edge discontinuities and non-uniform curvature on vortex formation and thrust production. It was demonstrated that the hydraulic diameter is the relevant length scale in collapsing the wake dynamics, and that plates of constant aspect ratio behave similarly. This work indicated that the presence of edges and non-uniform curvature play only a secondary role in vortex evolution during simple drag-based motions.

In the current study, a parameter space consisting of only elliptical flat plates with aspect ratios between one and two is considered. The goal of this study is to understand the ubiquity of propulsors with aspect ratios greater than one in species of diverse lineage and scale, employing both rowing and paddling swimming modes. Wainwright, Bellwood & Westneat (2002) investigated the pectoral-fin shape of 143 species of labrid fish (i.e. fish that create thrust through paired pectoral-fin rowing) and showed that less than 7% of the fish investigated were equipped with fins with aspect ratios less than 1.6. An overall inertial range corresponding to $Re = 10^3$ – 10^5 can be extracted from this study based on documented propulsor characteristics of each species. Similar biases towards planform aspect ratios greater than one have also been observed in the appendages of various semiaquatic species used for quadrupedal-, pectoral- and pelvic-based modes of paddling (Fish 1994, 1996, 2007).

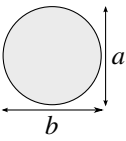
Geometry	Nomenclature	a (m)	b (m)	AR	Area (m ²)	Blockage (%)	D_h (m)
	E1	0.300	0.300	1	0.0707	7.07	0.3
	E2	0.315	0.287	1.1	0.0710	7.10	0.3
	E3	0.331	0.276	1.2	0.0719	7.19	0.3
	E4	0.382	0.255	1.5	0.0766	7.66	0.3
	E5	0.474	0.237	2	0.0884	8.84	0.3

TABLE 1. Relevant nomenclature and geometric characteristics of the elliptical plates. The aspect ratios of the plates are varied, while maintaining a constant hydraulic diameter.

Genera investigated in these linked studies encompass species of otters, platypuses, and muskrats, which are also characterized by propulsor Reynolds numbers between $Re = 10^3-10^5$. The work presented herein suggests that higher-aspect-ratio plates generate vortex rings with optimal thrust characteristics over a range of Reynolds numbers representative of the above taxa. The presentation of the manuscript is organized as follows. In § 2, the geometric characteristics of plates that have been investigated are discussed and tabulated. Thrust characteristics of each flat plate are investigated via direct comparisons of instantaneous drag-force data and an evaluation of vortex pinch-off using computed circulation-growth rates in § 3. The main conclusions of this study are then summarized in § 4.

2. Experimental methods

The following section provides a description of the five elliptical flat plates that were investigated, the techniques that were used in the measurements, and the facility where the measurements were performed.

2.1. Geometries tested

A parameter space consisting of elliptical flat plates with aspect ratios between one and two was investigated. The main characteristics of the five flat plates that were tested have been provided in table 1. These include the plate height (a), width (b), aspect ratio (AR), area, percent blockage of the tank cross-section, and length scale (D_h). Note that all flat plates are defined by a constant hydraulic diameter of 0.3 m.

2.2. Force and particle image velocimetry measurements

All experiments were performed in a towing-tank facility at Queen’s University which has a cross-sectional area of 1 m² and a total length of 15 m. The towing tank is equipped with a roof that runs along the entire length of the apparatus to minimize free-surface effects. Each plate underwent a motion consisting of an impulsive start from rest to the final towing velocity over a distance of half the characteristic length scale ($0.5D_h$), which is representative of non-dimensional acceleration periods observed in biological locomotion (Dickinson & Goetz 1993; Dickinson, Lehmann & Sane 1999). The motion was normalized using the following relationship:

$$s^* = \frac{s}{D_h}, \tag{2.1}$$

where s is the physical distance travelled and D_h is the hydraulic diameter. The plates were towed normal to the flow by mounting them perpendicular to a horizontal

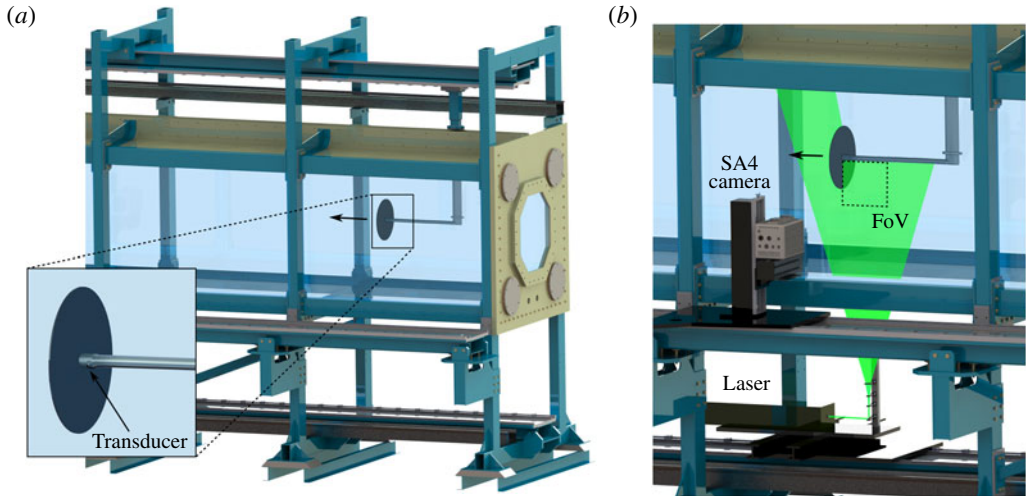


FIGURE 1. (a) Towing-tank facility depicting the circular flat plate at the beginning of the prescribed motion, and the location of the force transducer (shown in the inset); (b) the experimental set-up for PIV measurements, including the location of the high-speed camera and laser, and the approximate size and orientation of the field of view (FoV).

(cylindrical) sting, which has a diameter of $0.08D_h$ and a nominal length of $2D_h$. A section of the towing tank (approximately 3 m in length) is depicted in figure 1(a), along with the mounting configuration for the aspect-ratio-one plate. A six-component, submersible ATI Nano force transducer was mounted on the leeward side of the plates to record force data, and is depicted in the inset of figure 1(a). The transducer has a static resolution of $0.125N$ and was operated at a sampling rate of 1000 Hz. All data sets were averaged over 25 runs. Force measurements were acquired over a range of $50\,000 \leq Re \leq 350\,000$, at increments of $Re = 75\,000$ between each case, for a total of five cases. The Reynolds numbers were calculated using the terminal velocity of the plate and the hydraulic diameter.

Time-resolved planar particle image velocimetry (PIV) was used to measure vortex growth in the wake of the plates. A right-hand coordinate system was adopted such that the x -, y -, and z -axes are oriented in the streamwise, wall-normal, and spanwise directions, respectively. PIV measurements were undertaken for the aspect-ratio-one and aspect-ratio-two plates, for which the largest variation was observed in the drag-force histories; the remaining three plates exhibited intermediary behaviour. As such, the vortex dynamics associated with the two most disparate cases were characterized as a function of Reynolds number with velocimetry measurements in this study. The flow field was captured using a Photron SA4 high-speed camera, which has a resolution of 1024×1024 pixels, and was operated at frame rates of 200 and 1200 Hz. A 40 mJ pulse⁻¹ Photonics high-speed laser was used to create a laser sheet approximately 1.5 mm thick. The field of view (FoV) used for all measurements was approximately $1.3D_h \times 1.3D_h$ in size and was situated at the horizontal midspan of the plates (i.e. in the xy -plane) along the lower half of the sting, as shown in figure 1(b). Measurements were only recorded at the midspan of the minor axes for the aspect-ratio-two plate, as Fernando & Rival (2016) showed circulation-growth collapse at both the major and minor axes in their study. The towing motions were repeated and recorded 20 times for each FoV, and the results were phase-averaged.

Reynolds-number scaling of vortex pinch-off

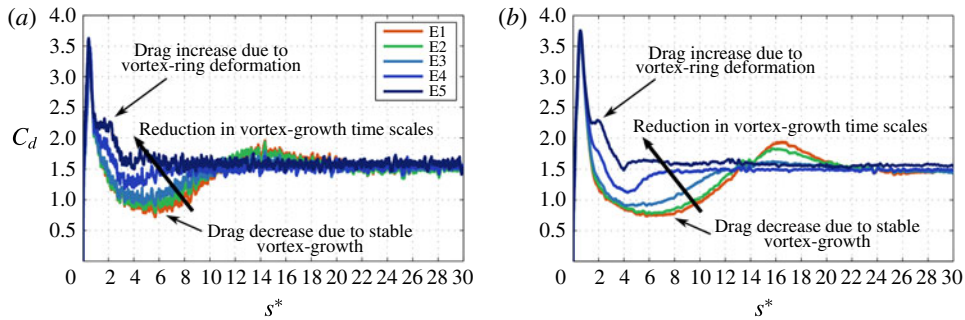


FIGURE 2. Comparison of the drag-coefficient history between all five elliptical flat plates, which demonstrates the gradual transition process between geometries at (a) $Re = 50\,000$ and (b) $Re = 350\,000$. The black arrows in (a,b) highlight the initial drag peak characteristic of high-aspect-ratio elliptical plates, the drag reduction due to stable vortex-ring growth in the wake of the aspect-ratio-one plate, and the transition process between these two distinct vortex–plate interactions for the intermediary plates.

3. Results and discussion

In this section, an overview of the instantaneous drag forces of each plate is first presented, followed by an investigation of vortex pinch-off. Both subsections are aimed at highlighting the relationship between vortex growth and Reynolds number.

3.1. Instantaneous forces

Vortex evolution has been shown to occur over two distinct time scales between plates with aspect ratio of one, and those with aspect ratios of two and greater (Fernando & Rival 2016). It is therefore reasonable to assume that a gradual transition process exists between plates over the range $1 \leq AR \leq 2$. Characterizing this transitional range is an important aspect of the current study. Since the time scales over which vortex evolution occurs are identifiable through the instantaneous drag-force data (i.e. the periods before the steady-state drag values are achieved), as shown by Fernando & Rival (2016), force measurements were first conducted for all five flat plates at the highest ($Re = 350\,000$) and lowest ($Re = 50\,000$) Reynolds numbers to elucidate this transitional region. Figure 2 contains two plots of the drag-coefficient history against dimensionless distance travelled. Since the drag forces exerted on the plates are analogous to thrust forces generated by propulsors, the drag coefficient may be viewed as a proxy for the thrust coefficient. Figure 2 illustrates the transition process from the drag reduction associated with the formation of circular vortex rings to the drag increase resulting from the highly transient behaviour of the unstable elliptical vortex rings that form in the wake of higher-aspect-ratio plates (Fernando & Rival 2016). The key features of the drag histories are highlighted in figure 2(a,b) with black arrows.

The Reynolds-number scaling of instantaneous drag forces was first investigated for the aspect-ratio-one and aspect-ratio-two plates, for which the greatest variation in vortex growth has been shown to exist within the parameter space. Dimensionless plots of the same format as figure 2 are provided in figure 3(a,b) for the aspect-ratio-two and aspect-ratio-one plates, respectively. For the aspect-ratio-two plate, collapse in the drag-force data is observed globally across the entire Reynolds-number

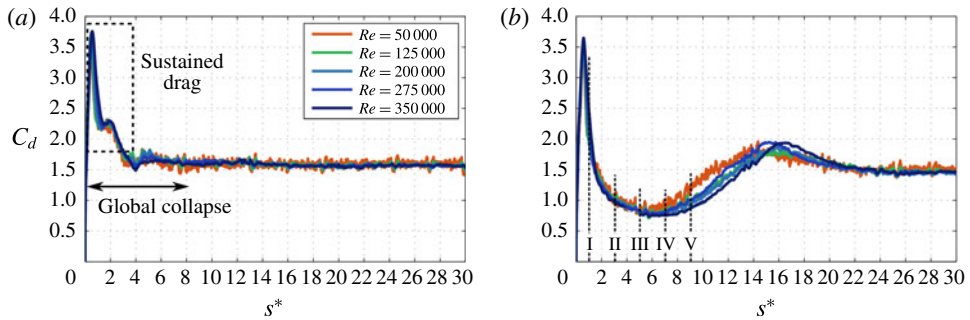


FIGURE 3. Drag-coefficient histories for the (a) aspect-ratio-two and (b) aspect-ratio-one plates for $50\,000 \leq Re \leq 350\,000$. Global collapse is observed of the aspect-ratio-two elliptical plate. In contrast, collapse is only observed between $s^* = 0-6$ for the aspect-ratio-one plate. The five Roman numerals indicate the time steps at which subsequent particle visualizations were performed.

parameter space investigated, as shown in figure 3(a). Large drag forces are exerted on the aspect-ratio-two plate for all Reynolds-number cases during the first four dimensionless distances of travel. This region is highlighted by the dashed box in figure 3(a). High, sustained periods of drag such as these are necessary for efficient forward propulsion. Collapse of the drag forces is observed only until approximately $s^* = 6$ for the circular plate, as shown in figure 3(b). After the initial acceleration, the drag force quickly decays towards a minimum at $s^* = 6$ as the vortex ring grows behind the plate. Fernando & Rival (2016) showed that the gradual increase in drag force after the global minimum at $s^* = 6$ is correlated with vortex-ring destabilization and subsequent breakdown. This drag increase, which is delayed with increasing Reynolds number, may therefore be interpreted as an indicator of relative vortex-ring stability. The five Roman numerals shown in figure 3(b) indicate the time steps at which vortex evolution was qualitatively investigated, as discussed subsequently.

To examine the claim of increased vortex-ring stability with increasing Reynolds number, particle visualizations were performed at $Re = 50\,000$ and $350\,000$ for the circular plate, and compared at key points during vortex growth, indicated by the Roman numerals in figure 3(b). Both halves of the vortex rings in a two-dimensional slice were visualized by offsetting the position of the laser a spanwise distance of $\Delta z/c = 0.05$ to avoid line-of-sight obstruction by the sting. Figures 4 and 5 contain visualizations that are representative of overall vortex evolution for both Reynolds numbers. Each image was generated by averaging ten subsequent frames at the desired instances in each FoV. For the lower Reynolds number, visualizations have been provided for approximate dimensionless distances of $s^* = 1, 3, 5$ and 7 in figure 4. The vortex rings at this Reynolds number were observed to become unstable at a dimensionless distance of approximately $s^* = 6$; the visualization in figure 4(d) illustrates the onset of detachment and breakdown. At the higher Reynolds number, visualizations are provided for dimensionless distances of $s^* = 1, 3, 5, 7$ and 9 in figure 5. As predicted from the force measurements, the vortex rings remain attached for longer (i.e. until approximately $s^* = 9$). Vortex breakdown begins later, at approximately $s^* = 10$. The black circles represent the approximate locations of the vortex cores, and demonstrate the increased convection of the vortex ring away from the plate prior to detachment. This is discussed in further detail later in this section.

Reynolds-number scaling of vortex pinch-off

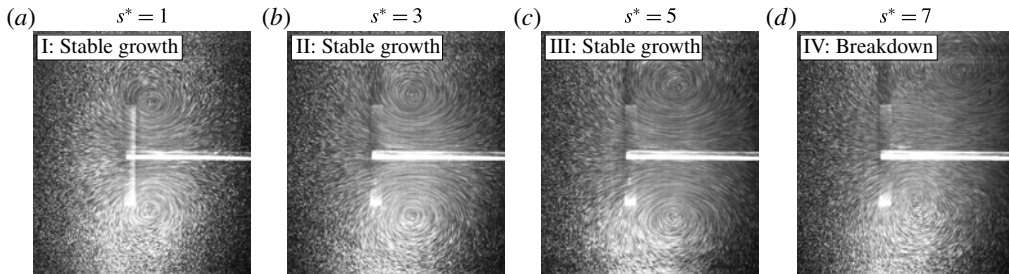


FIGURE 4. Particle visualizations for the aspect-ratio-one plate at $Re = 50\,000$. The vortex ring remains in close proximity to the plate during the first three time steps, but becomes unstable at approximately $s^* = 6$, and subsequently breaks down, as illustrated in the visualization in (d).

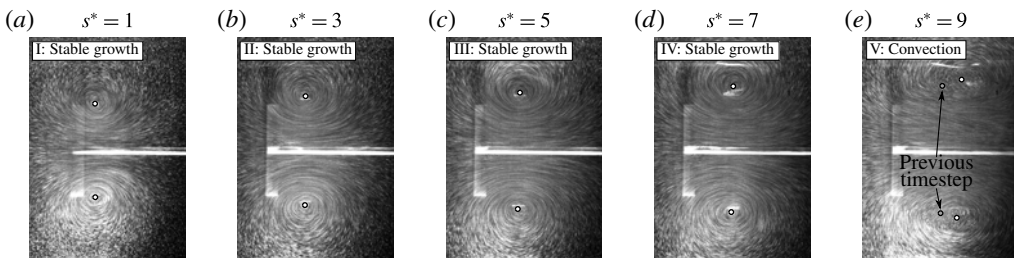


FIGURE 5. Particle visualizations for the aspect-ratio-one plate at $Re = 350\,000$. At this Reynolds number, the vortex ring remains stable and in close proximity to the plate until approximately $s^* = 9$, which marks the onset of breakdown, as shown in (e). The black circles mark the approximate vortex-core locations in each time step, and illustrate the increased convection of the vortex ring away from the plate in (e).

The drag histories in figure 3 suggest that Reynolds-number scaling may be directly related to the time scales of vortex growth. Force measurements were therefore undertaken at the highest and lowest Reynolds numbers for the remaining three geometries, which exhibit intermediary drag-force histories (refer to figure 2). The drag forces for the $AR = 1.1$, 1.2 and 1.5 plates are shown in figures 6(a), 6(b) and 6(c), respectively. If collapse in the drag-force data is primarily influenced by the time scales of vortex growth, then the force plots in figure 2 suggest that large sensitivity to Reynolds number can be expected for the $AR = 1.1$ plate, while good collapse is expected for the $AR = 1.5$ plate. This trend is clearly evident in figure 6.

The delayed vortex-ring breakdown with increasing Reynolds number for the circular plate is investigated qualitatively by closer inspection of the vortex-core topology during the growth phase. Previous work has shown that the transition of a laminar vortex ring to a turbulent vortex ring takes place via an azimuthal instability along the core (Maxworthy 1972). In particular, Maxworthy (1972) showed that along with the formation of this instability comes an overall reduction in the propagation speed of the vortex ring, since the self-induced velocities are no longer strictly parallel with the direction of bulk motion, but only have a velocity component in

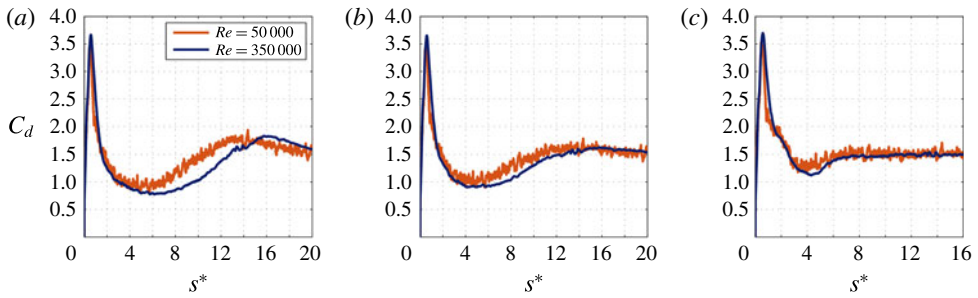


FIGURE 6. Drag-coefficient histories at the highest and lowest Reynolds numbers for the plates with aspect ratios of (a) 1.1, (b) 1.2, and (c) 1.5. The instantaneous drag force becomes less sensitive to Reynolds number with increasing aspect ratio.

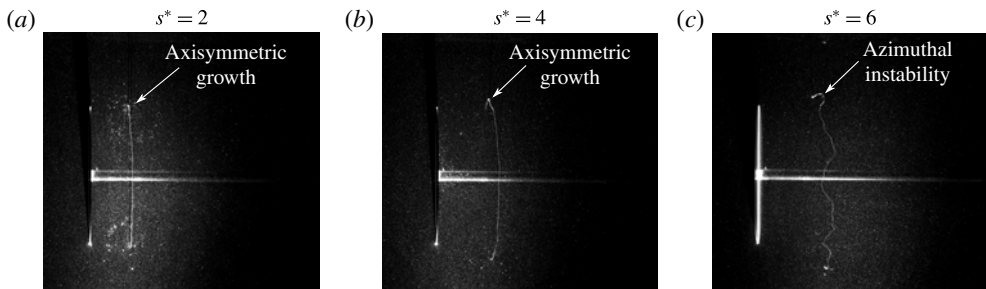


FIGURE 7. Hydrogen-bubble visualization of the vortex-core development at three time steps for the aspect-ratio-one plate at the highest Reynolds number ($Re = 350\,000$). During early-stage growth, the vortex core remains axisymmetric, as shown in (a,b). At approximately $s^* = 5$, an azimuthal instability develops along the core line, as indicated in (c) at a dimensionless distance of $s^* = 6$.

this direction. Instantaneous snapshots from visualizations similar to those used to generate the images in figures 4 and 5 were used to track the development of the vortex core. Hydrogen bubbles were created on the pressure side of the plate, which were entrained into the vortex and used to highlight the core. Visualizations at three time steps are shown in figure 7 for the highest Reynolds number. During early-stage growth, the vortex-core line remains axisymmetric, as shown in the visualizations in (a) and (b). By a dimensionless distance of approximately $s^* = 5$, an azimuthal instability develops, which persists and grows until the vortex ring detaches; the formation of this instability is exemplified in figure 7(c). The reduction in vortex-ring propagation speed reported by Maxworthy (1972) once an azimuthal instability has developed is qualitatively observed for the highest Reynolds-number case in figure 5. In figure 5(e), the approximate core locations from both the current and previous time step are shown, to qualify the movement of the vortex ring away from the plate. This convection away from the plate allows the vortex to remain attached while continuing to grow in size. The prolonged attachment of the vortex ring suggests that a vortex ring of greater overall strength will develop for the highest Reynolds-number case. This is investigated in the following section by computing vortex circulation and identifying when pinch-off occurs.

Reynolds-number scaling of vortex pinch-off

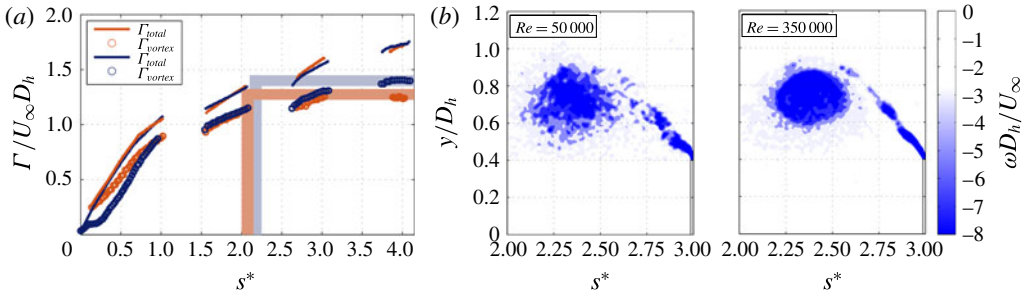


FIGURE 8. (a) Circulation growth for the aspect-ratio-two plate at the lowest (orange) and highest (blue) Reynolds numbers. Total circulation is indicated by solid lines, and vortex circulation is represented by hollow circles. The excellent collapse between the four curves suggests that vortex growth is insensitive to Reynolds number. The shaded bands represent the propagation of uncertainty in the vorticity fields to the evaluation of the formation numbers. (b) Phase-averaged vorticity magnitude plots for the lowest and highest Reynolds numbers (left and right, respectively) at $s^* = 3$, illustrating the topological similarities between the two cases.

3.2. Vortex pinch-off

Vortex pinch-off is investigated using the circulation-based methodology described by Gharib, Rambod & Shariff (1998). The total circulation emanating from the shear layer is computed as a function of time. Circulation growth of the vortex alone is then computed over the same time period. A plateau is observed in the vortex-circulation curve when the vortex is no longer able to accumulate vorticity-containing mass (i.e. when pinch-off has occurred). This maximum in circulation is related back to the curve of total circulation as follows. The instant where the value of total circulation matches the maximum circulation attained by the vortex is termed the ‘formation number’, and is a metric used to evaluate the time at which all vorticity supplied by the shear layer will eventually be accepted by the vortex. This methodology is demonstrated subsequently. Dimensionless circulation growth is plotted against dimensionless distance travelled in figure 8(a) for the aspect-ratio-two flat plate at both Reynolds numbers. Excellent collapse is observed in circulation growth in terms of both the total circulation in the system (solid lines) and vortex circulation (hollow circles), indicating that vortex pinch-off does not vary with Reynolds number for this geometry. The shaded blue and orange bars indicate the approximate plateau values of vortex circulation, which occur at approximately $s^* = 4$ for both Reynolds numbers. These values are projected back towards the total circulation curves to provide estimates of the formation numbers. Figure 8(b) consists of two phase-averaged vorticity magnitude plots for the lowest (left) and highest (right) Reynolds numbers at a time step of $s^* = 3$, which exemplify the nearly identical vortex topology between the two cases even after pinch-off has occurred.

For the aspect-ratio-one plate, circulation growth is plotted in figure 9(a,b) for the lowest and highest Reynolds numbers, respectively. In both cases, as the vortex rings grow in strength they remain in close proximity to the plates, such that the shear layer is nearly indiscernible from the vortex itself. Only after the vortex rings become unstable is there a clear distinction between the shear layer and the vortex, and pinch-off occurs shortly after. At $Re = 50,000$, pinch-off is estimated to occur at a dimensionless distance of approximately $s^* = 4.5$. Since the vortex ring that grows in

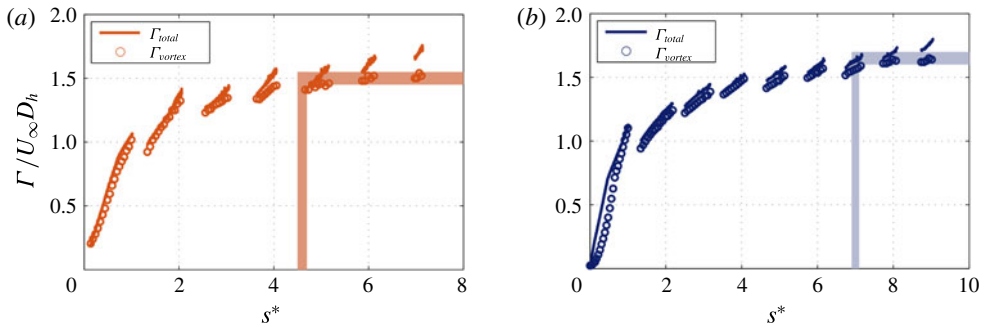


FIGURE 9. Circulation growth for the aspect-ratio-one plate at (a) $Re = 50\,000$ and (b) $Re = 350\,000$. Vortex pinch-off is estimated to occur at dimensionless distances of approximately $s^* = 4.5$ and $s^* = 7$ for the two cases, respectively, as indicated by the shaded bands.

the wake at the higher Reynolds number remains attached for longer, it has a greater final circulation, and pinch-off is delayed until an approximate value of $s^* = 7$. The formation numbers calculated here therefore reinforce the qualitative argument made from the particle visualizations that vortex-ring growth behind the aspect-ratio-one plate does not collapse with Reynolds number.

At the beginning of this section, instantaneous drag-force data for all five plates were used to demonstrate that the time scales of vortex formation gradually decrease with increasing aspect ratio. This has been further supported by evaluating vortex pinch-off for the aspect-ratio-one and aspect-ratio-two plates, and estimating much smaller vortex formation numbers for the aspect-ratio-two plate. This discrepancy can be attributed to the unstable behaviour of high-aspect-ratio elliptical vortex rings. Variation in local curvature has a primary impact on the induced velocities of a vortex ring (Green 2012). For the aspect-ratio-two plate, local curvature variation is severe enough that rapid deformations occur immediately after vortex formation. The results presented in this study suggest that this rapid deformation occurs over a time scale small enough that Reynolds-number effects can be neglected. However, local curvature changes become less severe with decreasing aspect ratio, and the forming vortices deform less rapidly. The force data in figure 6 suggest that an aspect ratio of 1.5 represents an approximate demarcation in Reynolds-number sensitivity. This is in excellent agreement with the studies undertaken by Fish (1994) and Wainwright *et al.* (2002), for example, which have documented the clear prevalence of high-aspect-ratio propulsors in diverse scales of biological locomotion.

4. Conclusions

Five elliptical flat plates with aspect ratios between one and two have been investigated to understand the specific vortex dynamics that may be optimized by propulsors found in nature during drag-based motions. Of particular interest to this study is the apparent evolutionary convergence of propulsors used in rowing and paddling kinematics towards planforms with aspect ratios greater than one. The rarity of propulsor planforms with aspect ratios close to one is well documented in the literature, but not well understood. In the current study it has been shown that for the elliptical flat plates with aspect ratios larger than one, large force peaks are observed during early-stage vortex growth, which are necessary for efficient

bursts of thrust during quick accelerations, and while turning and braking. For these higher-aspect-ratio plates, the drag forces and vortex dynamics have been shown to exhibit no variability with Reynolds number. This has been attributed to the strong variation in curvature associated with the high-aspect-ratio plates and forming vortex rings. Changes in local curvature along the vortex rings result in immediate vortex-ring deformation, and therefore growth time scales are small enough such that Reynolds-number effects may be neglected. The collapse of vortex pinch-off with Reynolds number for the aspect-ratio-two plate implies that species operating over disparate inertial scales may be utilizing the same optimal vortex dynamics. With decreasing aspect ratio, growth time scales gradually increase, and Reynolds-number effects can no longer be neglected. Therefore, no such collapse is observed for the aspect-ratio-one plate. Moreover, the stable (axisymmetric) vortex rings that form behind the aspect-ratio-one plate result in extended periods of reduced drag, which are detrimental during quick manoeuvres where large drag is desired for efficient locomotory control. The results presented in this paper therefore provide an explanation for the prevalence of propulsors with aspect ratios closer to two over the diverse biological scales in which they are observed.

Acknowledgements

The authors acknowledge the support from the United States Air Force Office of Scientific Research (AFOSR) under grant number FA9550-13-1-0117, monitored by Dr D. Smith.

References

- BLAKE, R. W. 1979 The mechanics of labriform locomotion. I: labriform locomotion in the angelfish (*Pterophyllum eimekei*): an analysis of the power stroke. *J. Expl Biol.* **82** (1), 255–271.
- BLAKE, R. W. 1981 Influence of pectoral fin shape on thrust and drag in labriform locomotion. *J. Zoology* **194** (1), 53–66.
- DICKINSON, M. H. & GOETZ, K. G. 1993 Unsteady aerodynamic performance of model wings at low Reynolds numbers. *J. Expl Biol.* **174**, 45–64.
- DICKINSON, M. H., LEHMANN, F.-O. & SANE, S. P. 1999 Wing rotation and the aerodynamic basis of insect flight. *Science* **284** (5422), 1954–1960.
- ELOY, C. 2013 On the best design for undulatory swimming. *J. Fluid Mech.* **717**, 48–89.
- FERNANDO, J. N. & RIVAL, D. E. 2016 On vortex evolution in the wake of axisymmetric and non-axisymmetric low-aspect-ratio accelerating plates. *Phys. Fluids* **28** (1), 017102.
- FISH, F. E. 1994 Influence of hydrodynamic-design and propulsive mode on mammalian swimming energetics. *Austral. J. Zoology* **42** (1), 79–101.
- FISH, F. E. 1996 Transitions from drag-based to lift-based propulsion in mammalian swimming. *Am. Zool.* **36** (6), 628–641.
- FISH, F. E. 2007 Diversity, mechanics and performance of natural aquatic propulsors. In *Flow Phenomena in Nature: A Challenge to Engineering Design*, vol. 1, p. 57. WIT Press.
- GAZZOLA, M., VAN REES, W. M. & KOUMOUTSAKOS, P. 2012 C-start: optimal start of larval fish. *J. Fluid Mech.* **698**, 5–18.
- GHARIB, M., RAMBOD, E. & SHARIFF, K. 1998 A universal time scale for vortex ring formation. *J. Fluid Mech.* **360**, 121–140.
- GREEN, S. I. 2012 *Fluid Vortices*. Springer Science & Business Media.
- HARTLOPER, C. & RIVAL, D. 2013 Vortex development on pitching plates with lunate and truncate planforms. *J. Fluid Mech.* **732**, 332–344.
- KIM, D. & GHARIB, M. 2011 Characteristics of vortex formation and thrust performance in drag-based paddling propulsion. *J. Expl Biol.* **214** (13), 2283–2291.

- LIGHTHILL, M. J. 1969 Hydromechanics of aquatic animal propulsion. *Annu. Rev. Fluid Mech.* **1**, 413–446.
- MAXWORTHY, T. 1972 The structure and stability of vortex rings. *J. Fluid Mech.* **51** (01), 15–32.
- VOGEL, S. 2013 *Comparative Biomechanics: Life's Physical World*. Princeton University Press.
- WAINWRIGHT, P. C., BELLWOOD, D. R. & WESTNEAT, M. W. 2002 Ecomorphology of locomotion in labrid fishes. *Environ. Biol. Fishes* **65** (1), 47–62.